Phase Balance and Performance of ER2209 Multilayer Deposits Produced by CMT with Nitrogen-Bearing Shielding Gas

Nilesh M. Bhangale[1], Dr. Bharat C. Khatri[2]*, Dr. Janak B. Valaki[3], Dr. Pravin P. Rathod[4], Dr. Pradip K. Gajjar[5]

[1]Research Scholar, Mechanical Department, Gujarat Technological University, Ahmedabad, 382424.

[2]Mechanical Engineering Department, L.D. College of Engineering, Ahemdad, 380015, Gujarat, India;

[3]Mechanical Engineering Department, Government Engineering College, Bhavnagar, 364001, Gujarat, India;

[4]Mechanical Engineering Department, Government Engineering College, Bhuj, 370001, Gujarat, India;

[5]Mechanical Engineering Department, Government Engineering College, Palanpur, 385001, Gujarat, India;

***Corresponding Author**

DOI: https://doi.org/10.51584/IJRIAS.2026.11090092

Received: 24 September 2026; Accepted: 29 September 2026; Published: 15 October 2026

ABSTRACT

Nitrogen-bearing shielding gases can influence phase transformation in duplex stainless-steel weld metal, but their effect in multilayer Cold Metal Transfer (CMT) deposition is also governed by heat input, interpass temperature, and repeated thermal cycling. In the present work, ER2209 multilayer deposits were produced under two shielding conditions, Ar + 2% N_2 and Ar + 5% N_2, over a practical range of welding current, voltage, travel speed, and wire-feed speed. The calculated heat input ranged from 0.648 to 1.283 kJ/mm, while the interpass temperature was maintained below 150 °C. The Ar + 5% N_2 processing group showed a markedly lower Ferrite Number, with mean values of 26.01 ± 0.64 FN compared with 35.49 ± 1.09 FN for the Ar + 2% N_2 group. This was the only response that showed a statistically significant difference between the two processing groups. Average hardness remained almost unchanged at 262.22 ± 6.25 and 263.68 ± 7.84 HV10, respectively. Mean impact energy at 0 °C was higher for the Ar + 5% N_2 group, increasing from 77.6 ± 11.95 to 88.8 ± 7.56 J, although the difference was not statistically significant. Pitting-test mass loss differed only slightly between the groups, whereas crevice-test mass loss was lower on average for the Ar + 5% N_2 condition. Optical microscopy supported the observed change in phase balance. Since shielding-gas composition was varied together with deposition parameters and layer count, the results are interpreted as differences between overall processing conditions rather than as an isolated effect of nitrogen concentration. The findings indicate that phase balance was more sensitive to the processing condition than hardness or corrosion mass-loss response and highlight the need for matched-parameter experiments to establish the independent effect of shielding-gas nitrogen.

Keywords: Duplex stainless steel; ER2209; Cold Metal Transfer; wire arc additive manufacturing; nitrogen-bearing shielding gas; ferrite number;

INTRODUCTION

Duplex stainless steels obtain their engineering properties from a two-phase ferrite–austenite microstructure, which provides a combination of relatively high strength, useful toughness and resistance to chloride-induced localized corrosion. This phase balance is strongly affected by welding because the material solidifies mainly as ferrite, with austenite forming during subsequent cooling. As a result, the final phase constitution is controlled

not only by alloy chemistry, but also by the peak temperature reached, the cooling rate and the time available for ferrite-to-austenite transformation[1]. In multilayer deposition, this relationship becomes more complex because previously solidified material undergoes repeated reheating from subsequent passes. Local phase evolution consequently reflects a sequence of thermal cycles rather than a single weld-cooling event[2], [3].

Nitrogen plays a particularly important role in this transformation. As a strong austenite-stabilizing element, nitrogen promotes ferrite-to-austenite transformation and can partly compensate for nitrogen loss from the molten weld pool. It also contributes to localized-corrosion resistance through its influence on phase chemistry and passive-film stability. Studies on conventionally welded duplex stainless steels have shown that nitrogen-bearing shielding gases can promote austenite formation and modify localized-corrosion behaviour [4]–[7]. The response is not necessarily monotonic, however. Nitrogen absorption depends on shielding-gas composition, arc characteristics, heat input and the thermodynamic and kinetic conditions of the molten pool[8]. A recent mechanised-GMAW study further demonstrated that shielding-gas composition and the associated welding thermal conditions jointly influenced nitrogen retention, ferrite–austenite balance, hardness and localized-corrosion performance of super-duplex stainless-steel overlays[7]. At the same time, excessive nitrogen availability or an unfavourable thermal cycle may promote nitride formation or other microstructural changes that adversely affect toughness and corrosion performance. Shielding-gas nitrogen must therefore be considered together with the thermal conditions established during deposition[4], [9].

These interactions become particularly significant in wire arc additive manufacturing (WAAM) and related directed-energy-deposition processes. Although arc-based additive manufacturing offers high deposition rates and is attractive for producing large metallic components, successive layer deposition creates repeated reheating, thermal accumulation and spatially varying cooling conditions. Hosseini et al. reported that arc energy and interlayer thermal history affect austenite formation and the development of secondary phases in additively manufactured duplex stainless steel[2]. Studies on CMT-based WAAM have also shown that microstructure, texture and mechanical behaviour can vary with build height and specimen orientation[10], [11]. For this reason, the metallurgical condition of a multilayer deposit cannot be assessed only from the nominal heat input; the thermal history accumulated during the build also needs to be taken into account[12]–[15]. The importance of heat input has also been demonstrated in conventional stainless-steel welding, where changes in welding thermal conditions affected microstructure, hardness, tensile behaviour and susceptibility to intergranular corrosion[16].

Filler-metal chemistry is another factor that needs to be considered. ER2209-type welding consumables contain more nickel than commonly used 2205 duplex stainless-steel base materials and are designed to support sufficient austenite formation in the weld metal. Previous studies on duplex-stainless-steel WAAM have shown that filler composition, travel speed, wire-feed speed and heat input collectively affect wall geometry, phase balance and mechanical response. Accurate identification of the welding consumable is therefore essential when interpreting the influence of shielding-gas composition. In the present work, multilayer walls were deposited using a certified ER2209-class filler wire, and the investigation focuses on the behaviour of the deposited material[17], [18].

Recent investigations provide useful context for evaluating nitrogen enrichment during CMT processing. Zhang et al. examined shielding gases containing 0–6% N_2 during CMT-pulse hybrid welding of duplex stainless steel and reported enhanced austenite formation with nitrogen addition. However, the increase became less pronounced at higher nitrogen levels, while impact toughness reached its maximum at an intermediate nitrogen concentration [9]. More recently, Tóth et al. reported enhanced austenite formation during DED-arc fabrication using nitrogen-bearing shielding gas, while also demonstrating the importance of arc power and travel speed [19]. These observations indicate that the effect of nitrogen cannot be separated from the processing window and that a higher nitrogen concentration should not automatically be regarded as universally advantageous.

Despite the growing literature on duplex-stainless-steel welding and WAAM, comparatively limited information is available on the combined metallurgical, mechanical and localized-corrosion response of **ER2209 multilayer deposits produced by CMT under different nitrogen-bearing shielding conditions**. In particular, direct comparisons combining Ferrite Number, optical microstructure, chemical composition, hardness, impact behaviour and ASTM G48 corrosion response within the same experimental campaign remain limited.

ISSN No. 2454-6194 | DOI: 10.51584/IJRIAS |Volume XI Issue IX September 2026

Establishing these relationships is important because changes in phase balance may influence different properties to different extents.

Accordingly, the present study compares ten multilayer CMT deposits produced under nominal **Ar + 2% N_2** and **Ar + 5% N_2** shielding conditions. The investigation considers deposition geometry, optical microstructure, Ferrite Number, chemical composition, Vickers hardness, impact energy, tensile behaviour, ASTM G48 pitting- and crevice-test mass loss, and radiographic quality assessment. Because welding current, arc voltage, travel speed, wire-feed speed and layer count varied across the experimental matrix, the measured responses are interpreted as the combined outcome of shielding-gas composition and CMT processing conditions rather than as an isolated effect of nitrogen concentration. The study therefore aims to determine whether the two processing groups exhibit consistent differences in phase balance and performance, to identify which responses are most sensitive to the processing condition, and to relate the observed behaviour to the thermal and metallurgical characteristics of multilayer CMT deposition More generally, thermomechanical manufacturing studies have shown that changes in processing direction and process parameters can significantly alter microstructure, hardness and mechanical response[20]–[22].

MATERIALS AND EXPERIMENTAL METHODOLOGY

Material system and filler wire

The multilayer walls were deposited using **Exaton 22.8.3.L duplex stainless-steel wire** supplied by ESAB. According to the manufacturer's inspection certificate, the consumable was classified as **SFA/AWS A5.9 ER2209, EN ISO 14343-A G/W/P 22 9 3 N L,** and **EN ISO 14343-B 2209.** The wire had a diameter of **1.2 mm.** Its certified composition is given in Table 1, with **23.1 wt.% Cr, 8.6 wt.% Ni, 3.0 wt.% Mo and 0.16 wt.% N** as the main alloying elements. The same certificate also listed a **WRC-92 Ferrite Number of 53** and a **PRE value of 35.6.** These values characterize the supplied filler wire lot and are used here only as feedstock information; they should not be interpreted as properties measured from the deposited CMT walls.

The walls were deposited on stainless-steel substrate plates that were positioned on supporting plates, tack welded at several locations and secured to the worktable using **C-clamps** to restrict movement during deposition. A representative set of the fabricated multilayer walls and the fixture arrangement is shown in Fig. 1. The available experimental records identify the substrate as stainless steel but do not provide a traceable material certificate specifying its exact grade and chemical composition. Consequently, substrate chemistry is not included as a variable in the comparison between the two shielding-gas processing groups. Any possible substrate-dilution effect is expected to be most relevant near the initial deposited layers and is considered when interpreting composition and microstructure close to the wall–substrate interface.

Table 1. Chemical composition of the certified ER2209 filler wire used in the experimental programme.

C	Si	Mn	P	S	Cr	Ni	Mo	Nb	Cu	N	W	FN	PRE
0.014	0.48	1.5	0.018	0.001	23.1	8.6	3.0	0.01	0.1	0.16	0.03	53	35.6

Multilayer deposition was performed using a robot-assisted Cold Metal Transfer (CMT) system consisting of a Fronius TPS 400i power source, Fronius welding torch and wire-feeding unit, and an ABB robotic motion system. The shielding-gas flow rate was maintained at 20 L/min throughout deposition.

Two nitrogen-bearing shielding-gas conditions were investigated: Ar + 2% N_2 and Ar + 5% N_2. The certified composition of the latter mixture was 4.99% N_2 with Ar as the balance gas, which is consistent with the nominal 5% N_2 specification. The Ar + 2% N_2 condition is reported according to its nominal supplied composition because an analytical certificate for this mixture was not available for verification. Five multilayer walls were fabricated under each shielding condition. The Ar + 2% N_2 walls consisted of 18 deposited layers, whereas the Ar + 5% N_2 walls consisted of 20 layers.

ISSN No. 2454-6194 | DOI: 10.51584/IJRIAS |Volume XI Issue IX September 2026



Fig. 1. Representative fabrication record: (a) plate/support arrangement prior to deposition and (b) completed multilayer wall builds (coupon Number 1 to 5 from left to right.

The welding current, arc voltage, travel speed and wire-feed speed were varied across the experimental matrix rather than held at identical values for the two shielding-gas groups as shown in Table 2. The experiments therefore represent two CMT processing groups incorporating different shielding atmospheres and deposition conditions. Accordingly, subsequent comparisons are interpreted in terms of the combined processing condition rather than as an isolated quantitative effect of increasing the shielding-gas nitrogen concentration from 2% to 5%.

Table 2. CMT process welding variable for 10 coupons.

Coupon ID	Current (A)	Voltage (V)	Travel speed (mm/min)	WFS (m/min)	Shielding gas	Heat input (kJ/mm)	Layers
1	140	14	140	5.8	Ar + 2% N_2	0.756	18
2	140	15	160	6.8	Ar + 5% N_2	0.709	20
3	155	17	120	5.8	Ar + 5% N_2	1.186	20
4	155	16	200	4.8	Ar + 2% N_2	0.67	18
5	170	12	160	8.8	Ar + 2% N_2	0.689	18
6	170	14	180	4.8	Ar + 5% N_2	0.714	20
7	190	15	120	7.8	Ar + 2% N_2	1.283	18
8	190	16	140	8.8	Ar + 5% N_2	1.173	20
9	200	17	180	6.8	Ar + 2% N_2	1.02	18
10	200	12	200	7.8	Ar + 5% N_2	0.648	20

ISSN No. 2454-6194 | DOI: 10.51584/IJRIAS |Volume XI Issue IX September 2026

Heat input and interpass-temperature control

The nominal heat input for each deposition condition was calculated from the machine-set welding current and arc voltage, the programmed travel speed, and an assumed process-efficiency factor of $\eta = 0.90$, according to $= 60\frac{\eta V I}{1000\, v}$,where H is the calculated heat input (kJ/mm), V is the arc voltage (V), II is the welding current (A), and v is the travel speed (mm/min). Using this approach, the calculated heat input across the ten deposition conditions ranged from **0.648 to 1.283 kJ/mm as shown in** Fig. 2. The value of $\eta = 0.90$ was used as a calculation factor for all experiments and should not be interpreted as an experimentally measured thermal efficiency. Current and voltage correspond to the values entered into the Fronius machine power source and checked on the display; time-resolved electrical signals were not independently acquired. The calculated heat-input values are therefore used as comparative process descriptors rather than direct measurements of the instantaneous thermal energy transferred to the deposit.

Interpass temperature was controlled after each deposited layer using 150 °C temperature-indicating thermal chalk which is shown in Fig. 3. The top surface of the wall was checked at three locations before deposition of the subsequent layer, and deposition was resumed only after the monitored locations satisfied the prescribed 150 °C interpass-temperature criterion. The thermal chalk was used as a threshold indicator rather than as a continuous temperature-measurement device. This procedure was applied throughout multilayer fabrication to limit excessive heat accumulation between successive deposition passes.

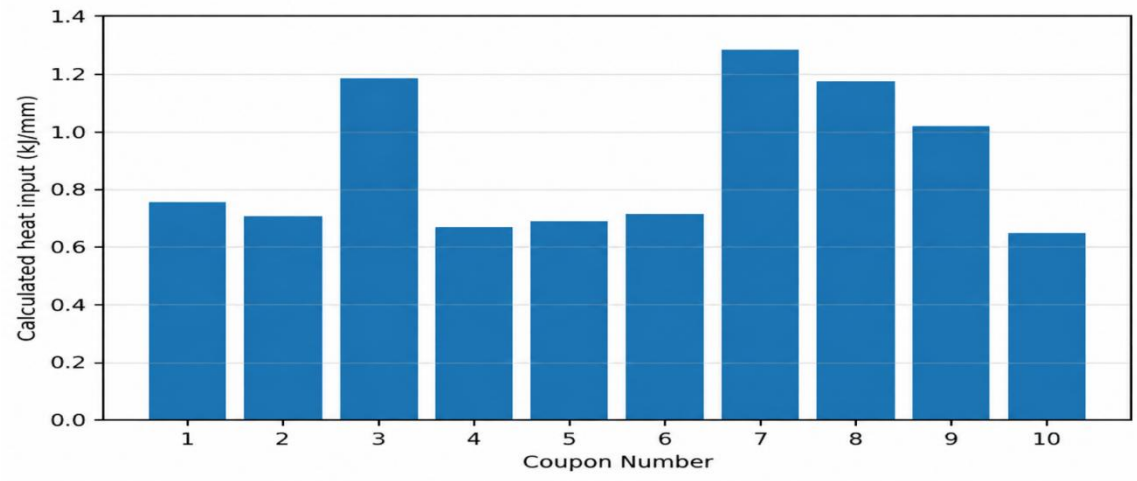

Fig. 2. Calculated heat input fo1r the ten deposition runs of Ten coupons.



Fig. 3. 150 °C temperature-indicating thermal chalk used for interpass-temperature control during multilayer deposition.

Geometrical characterization

Final wall geometry was characterized after completion of the multilayer deposition. **Wall width** was measured using a dial caliper, while **build height** was measured from the substrate surface to the crown of the deposited

wall using a graduated steel rule. Measurements were taken at several positions along the wall length to account for longitudinal variation in the deposited geometry. Representative measurement locations are shown in Fig. 4. The reported wall width and build height were used as overall geometrical responses of the completed multilayer deposits.



Fig. 4. Representative geometrical measurements: (a) final wall width using a dial caliper and (b) build height using a graduated steel rule.

The 18-layer Ar + 2% N_2 walls exhibited final widths of **13.03–14.07 mm** and build heights of **51.00–54.67 mm**, whereas the 20-layer Ar + 5% N_2 walls exhibited widths of **11.49–14.48 mm** and heights of **56.00–66.33 mm**. Because the two groups were produced using different process settings and different numbers of deposited layers, the measured dimensions reflect the overall deposition conditions rather than the effect of shielding-gas nitrogen concentration alone.

Metallographic preparation and optical microscopy

Metallographic specimens were sectioned from the deposited wall material and prepared by conventional grinding and polishing followed by etching prior to optical examination. Microstructural observations were carried out at nominal magnifications of **200X and 500X**, with corresponding scale bars of **100 µm and 50 µm**, respectively. Optical microscopy was used to examine the morphology and distribution of the duplex constituents and to compare qualitative microstructural differences between the two processing groups.

The optical images were interpreted qualitatively and were not used to determine numerical ferrite/austenite phase fractions. Accordingly, elemental partitioning, crystallographic texture, and the presence or identity of fine secondary phases were not inferred from optical contrast alone. Quantitative comparison of phase balance was instead based on the **Ferrite Number measurements** described in Section 2.6.

Ferrite Number measurement

Ferrite Number (FN) was measured using a **Fischer FERITSCOPE** in accordance with the laboratory procedure reported as **ASTM A800/A800M-20** [6]. For each deposited coupon, **eight measurements** were taken at randomly selected locations on the top surface of the wall on coupon shown Fig. 5(a) & Fig. 5(b), and the arithmetic mean of the eight readings was used as the representative FN for that specimen. The repeated measurements were used to capture local variation across the deposited surface, while the deposited build was treated as the independent experimental unit for comparison between the two shielding conditions (n=5 per group).

Because Ferrite Number is derived from the magnetic response of the material rather than from direct stereological measurement, the results are reported as **FN** and are not converted into ferrite volume percentage. ISO 8249:2018 provides a weld-metal-specific framework for Ferrite Number measurement in austenitic and duplex ferritic-austenitic stainless-steel weld metals; however, it is cited here only for context and is not claimed as the laboratory test method used in the present work.

ISSN No. 2454-6194 | DOI: 10.51584/IJRIAS |Volume XI Issue IX September 2026



5(a)

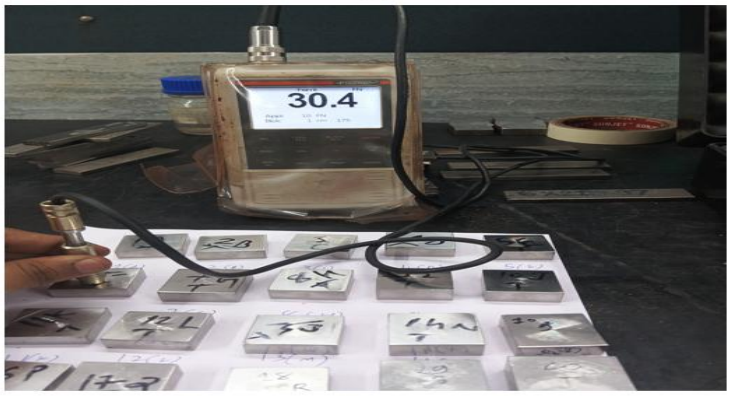

5(b)

Fig. 5.a Test coupon photo ready for ferrite measurement b. Fischer FERITSCOPE used for top-surface Ferrite Number measurements (10test coupons were extracted from the 10 welded coupons).

Mechanical testing

Tensile testing

Machined solid-round tensile specimens were prepared from the deposited wall material with initial diameters of approximately **6.19–6.45 mm** and an initial gauge length of approximately **25 mm**. Tensile testing was carried out using a **25 mm extensometer gauge length** and a crosshead-travel rate of **5 mm/min**. The measured outputs included **0.2% proof stress, ultimate tensile strength (UTS), elongation, reduction in area, peak load, and final specimen dimensions**. The various test coupon was extracted from the welded coupon as shown in Fig.6.

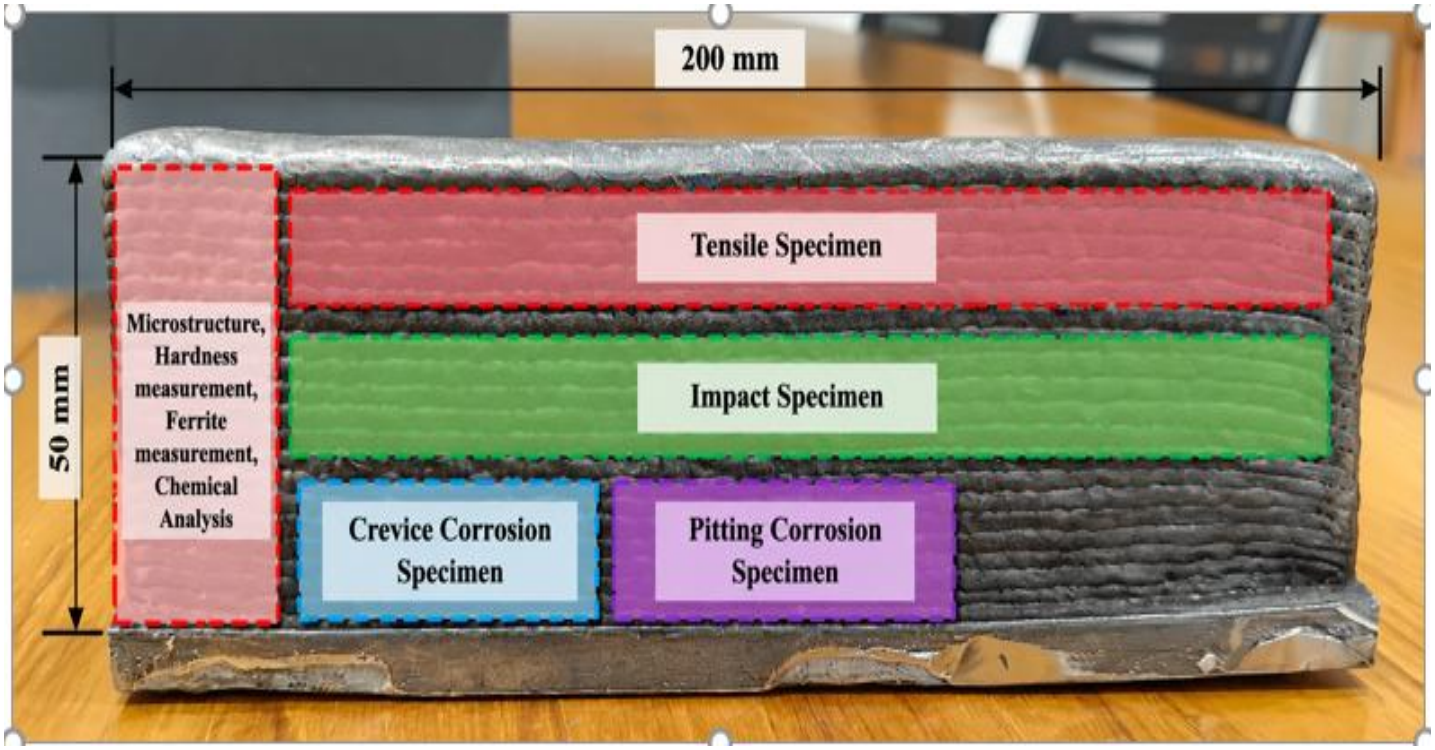

Fig. 6. Location of the various test coupons (from bottom plate 5 mm part is removed to avoid the effect of dilution)

ISSN No. 2454-6194 | DOI: 10.51584/IJRIAS |Volume XI Issue IX September 2026

Vickers hardness

Vickers hardness measurements were performed using an **FIE Vickers hardness testing machine** in accordance with **ASTM E92-23**. Hardness was reported on the **HV10 scale**. For each deposited coupon, measurements were obtained at **eight selected layer positions**, with **three indentations performed at each layer**. The three readings were averaged to obtain the representative hardness for that layer, and the eight layer averages were subsequently used to calculate the coupon-level hardness. Thus, each reported coupon average represents **24 individual hardness measurements**, providing information on hardness variation through the multilayer deposit.

Impact testing

Notched-bar impact testing was performed in accordance with **ASTM E23-25**. The specimens measured **55 × 5 × 10 mm** and were tested at **0 °C as shown in Fig.7**. One absorbed-energy value was obtained for each of the ten specimens and reported in joules (J). Because the available laboratory record does not specify the notch orientation or specimen extraction direction, the impact results are used primarily for **comparative assessment between the two processing groups** rather than for orientation-specific toughness characterization.



Fig. 7. Mechanical-test equipment used in the experimental campaign: (a) FIE Vickers hardness machine and (b) pendulum impact-testing machine.

Pitting and crevice corrosion testing

Pitting- and crevice-corrosion behaviour was evaluated using **ASTM G48 ferric-chloride exposure testing** [23]. For each specimen, the initial mass and exposed surface area were recorded before testing. After completion of the corrosion exposure, the specimens were cleaned, dried and reweighed to determine the mass loss. The corrosion response was normalized by the exposed area and reported as **mass loss per unit area (g/m²)**, with lower values representing less material loss under the applied test condition. The specimen surfaces were further examined at approximately **20× magnification** after the test to check for visible signs of localized attack. Since the laboratory record does not provide the exact ASTM G48 method designation, exposure temperature, test duration or solution-preparation details, the results are considered only as comparative mass-loss data. They are therefore not used to determine critical pitting temperature, critical crevice temperature or electrochemical breakdown parameters.

Chemical composition analysis

Chemical composition of the deposited specimens was determined using a **Bruker optical-emission spectrometer (OES)**. OES results were used to assess compositional consistency among the deposited walls and to examine variations in the principal alloying elements as shown in Fig.8. Because nitrogen was reported by the laboratory as part of the instrumental output but is not among the principal analytes covered by ASTM E1086-22, the measured nitrogen values are treated as **supporting compositional data** rather than as direct quantitative evidence of nitrogen uptake from the shielding atmosphere.

ISSN No. 2454-6194 | DOI: 10.51584/IJRIAS |Volume XI Issue IX September 2026



Fig. 8. Bruker optical-emission spectrometer used for chemical-composition analysis.

Radiographic examination

Radiographic testing was carried out as an internal-quality screening step before destructive characterization of the deposited walls. The radiographs covered the deposited length between the marked end locations and included image-quality indicators within the exposure field. The available films were examined for evidence of gross volumetric discontinuities, including extensive porosity, large inclusions and other major internal imperfections. Because the available records do not specify the radiographic testing standard, radiation source and energy, sensitivity determination or formal acceptance criteria, the RT results are used only as a qualitative quality-control check. Radiography is therefore not treated as a quantitative response variable, and no code-based acceptance or compliance statement is made from the film images alone.

Data treatment and scope of inference

Five deposited builds were considered for each shielding-gas processing condition (n = 5 per group). Repeated measurements obtained from the same specimen were treated as within-specimen observations rather than independent experimental replicates; therefore, the eight Ferrite Number measurements and multiple Vickers hardness indentations were first averaged at specimen level before calculating group statistics. Coupon-level responses were compared between the Ar + 2% N_2 and Ar + 5% N_2 processing groups using Welch's independent-samples t-test, which does not assume equal population variances. Statistical significance was evaluated at $\alpha = 0.05$. The independent experimental unit was the deposited build, not each repeated measurement. Because welding current, arc voltage, travel speed, wire-feed speed and layer count were not matched between the two shielding-gas groups, statistical significance was interpreted only as evidence of a difference between the complete processing groups and not as proof of a causal nitrogen-concentration effect. The results are therefore discussed in terms of measured associations, while mechanistic interpretations are related to established duplex-stainless-steel metallurgy and relevant literature.

RESULTS

Processing window and wall geometry

Multilayer deposition was completed over the full programmed processing window of **140–200 A, 12–17 V, 120–200 mm/min travel speed, and 4.8–8.8 m/min wire-feed speed**. The calculated heat input varied from 0.648 to 1.283 kJ/mm, giving almost a two-fold difference across the experimental conditions. This variation can affect melt-pool size, bead spreading, solidification behaviour and cooling rate, together with the thermal accumulation produced during successive layer deposition.

The final wall dimensions also varied with the processing conditions. For the Ar + 2% N_2 group, wall width ranged from **13.03 to 14.07 mm** and build height from **51.00 to 54.67 mm**. The Ar + 5% N_2 group showed wall widths of **11.49–14.48 mm** and build heights of **56.00–66.33 mm**. The greater height measured for the Ar + 5% N_2 walls should not be attributed to the shielding gas alone, since these walls contained **20 layers**, whereas the Ar + 2% N_2 walls contained **18 layers**. The wider spread in wall width for the Ar + 5% N_2 group may also be related to differences in travel speed, wire-feed speed, electrical parameters, wetting behaviour and accumulated

ISSN No. 2454-6194 | DOI: 10.51584/IJRIAS |Volume XI Issue IX September 2026

thermal history. Previous studies on duplex-steel WAAM have similarly reported that travel speed, wire-feed speed and heat input influence the final wall geometry[18].

Chemical composition of the deposited material

Table 3. chemical result of the test coupon (wt.%).

ID	C	Si	S	P	Mn	Ni	Cr	Mo	N*	Cu
1	0.0042	0.559	0.0029	0.016	1.538	8.567	21.66	2.838	0.107	0.207
2	0.0047	0.568	0.0027	0.017	1.472	8.562	21.56	2.88	0.106	0.207
3	0.0076	0.579	0.0029	0.016	1.527	8.499	21.7	2.799	0.11	0.203
4	0.017	0.579	0.0028	0.016	1.5	8.528	21.61	2.829	0.107	0.205
5	0.0051	0.578	0.0029	0.017	1.518	8.495	21.61	2.804	0.107	0.207
6	0.0094	0.583	0.0029	0.014	1.495	8.604	21.58	2.875	0.086	0.217
7	0.0085	0.574	0.0028	0.013	1.5	8.601	21.81	2.854	0.084	0.222
8	0.0052	1.467	0.003	0.012	1.467	8.543	21.8	2.823	0.083	0.219
9	0.0063	0.571	0.0027	0.012	1.446	8.522	21.68	2.817	0.082	0.223
10	0.0059	0.568	0.0028	0.017	1.465	8.579	21.93	2.793	0.107	0.205

The main alloying elements changed only slightly among the ten deposited specimens can be observed in the table 3. Chromium was measured between 21.56 and 21.93 wt.%, nickel between 8.495 and 8.604 wt.%, and molybdenum between 2.793 and 2.880 wt.%. These narrow ranges show that the Cr–Ni–Mo composition remained broadly similar throughout the experimental set. Carbon, sulfur and phosphorus were also present at low levels. One silicon value of 1.467 wt.% was much higher than the approximately 0.56–0.58 wt.% recorded for the other specimens. Since this value is clearly different from the rest of the results, it has been retained as reported but is not used for further mechanistic discussion. Nitrogen content can be seen in the Fig. 9 compared with different ten coupons and which was <0.16 less than to filler wire content.

The nitrogen values reported by the laboratory ranged from 0.082 to 0.110 wt.%, which is below the 0.16 wt.% N given in the ER2209 filler-wire certificate. This reduction in the deposited material may be related to molten-pool reactions, dilution, thermal history and the position from which the sample was taken. These nitrogen values, however, need to be considered with caution because the two shielding-gas groups were produced under different processing conditions, and nitrogen is not listed among the principal analytes covered by ASTM E1086-22. The OES results are therefore used mainly to describe the overall chemical consistency of the deposits and not as direct proof of increased nitrogen absorption under the Ar + 5% N_2 shielding condition.

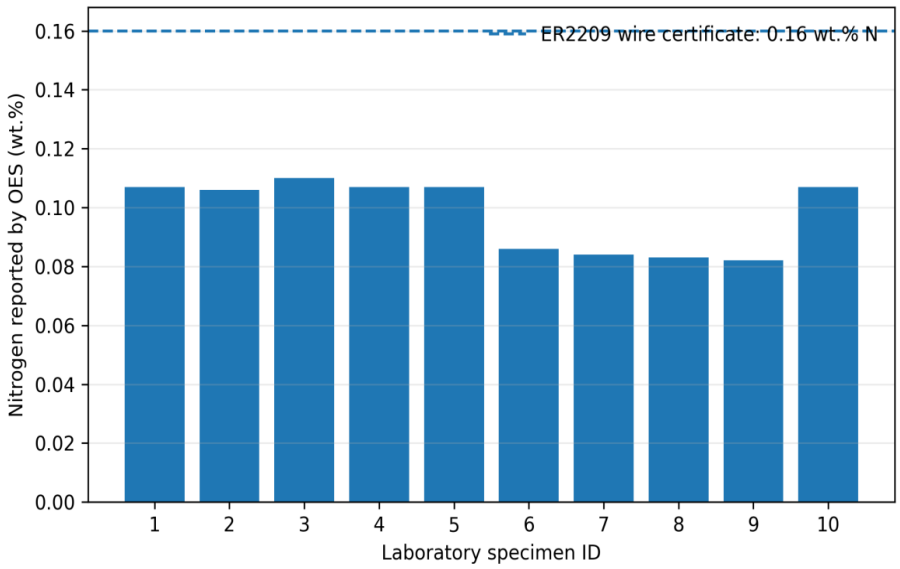

Fig. 9. Nitrogen content reported by OES for Coupon 1–10.

ISSN No. 2454-6194 | DOI: 10.51584/IJRIAS |Volume XI Issue IX September 2026

Ferrite Number

Ferrite Number provided the most distinct difference between the two processing groups. For the five specimens produced with Ar + 2% N_2, the mean FN values ranged from 34.35 to 37.07, with an overall average of 35.49 ± 1.09 FN. The Ar + 5% N_2 specimens gave lower mean values, ranging from 25.20 to 26.80 FN, with an overall average of 26.01 ± 0.64 FN. There was no overlap between the coupon-level ranges, and the mean FN of the Ar + 5% N_2 processing group was approximately 26.7% lower. Welch's independent-samples t-test confirmed a statistically significant difference between the two processing groups ($t = 16.76$, $p < 0.001$). Because shielding-gas composition was not isolated from the other process variables, this statistical result demonstrates processing-group separation but does not establish nitrogen concentration as the sole cause of the FN difference. The detailed FN readings are given in Table 4.

Each coupon-level value represents the arithmetic mean of eight measurements obtained at randomly selected locations on the top surface of the deposited wall. The consistent separation across these distributed measurements indicates that the processing-group difference in FN was not associated with a single localized reading. Rather, a systematic shift toward lower Ferrite Number was observed for the Ar + 5% N_2 processing condition, as shown in Fig. 10.

The optical micrographs showed the characteristic heterogeneous duplex morphology of the deposited material and qualitatively supported the difference indicated by the FN measurements. However, the optical images were not used to calculate numerical ferrite or austenite fractions because optical contrast can be affected by etching response, section orientation and local position within the multilayer wall. Accordingly, the quantitative phase-balance comparison in the present study is based on **Ferrite Number**, while optical microscopy is used as supporting evidence for differences in microstructural morphology.

Table 4. Ferrite Number measurements. Each coupon mean is based on eight random top-surface readings.

Coupon Number	**Eight FN readings**	**Mean FN**	**Mean FN ± SD**	**Range**
1 Ar + 2% N_2	34.3, 36.9, 34.4, 33.1, 35.9, 35.4, 36.1, 36.8	35.36		
2 Ar + 2% N_2	33.6, 38.2, 34.2, 36.6, 37.1, 37.8, 35.4, 35.2	36.01		
3 Ar + 2% N_2	33.1, 33.3, 35.2, 34.8, 35.6, 33.7, 36.4, 35.2	34.66	35.49 ± 1.09	34.35–37.07
4 Ar + 2% N_2	34.3, 32.6, 33.4, 32.5, 35.1, 35.7, 34.8, 36.4	34.35		
5 Ar + 2% N_2	36.5, 37.8, 35.1, 36.4, 39.3, 38.1, 36.3, 37.1	37.07		
6 Ar + 5% N_2	25.7, 26.5, 28.0, 26.9, 30.3, 26.5, 25.1, 25.4	26.8		
7 Ar + 5% N_2	25.9, 24.2, 26.6, 27.5, 24.2, 25.6, 25.1, 28.3	25.92		
8 Ar + 5% N_2	24.3, 28.0, 26.1, 27.3, 24.4, 25.3, 28.1, 28.3	26.47	26.01 ± 0.64	25.20–26.80
9 Ar + 5% N_2	23.5, 23.9, 24.1, 25.3, 26.4, 25.2, 27.4, 25.8	25.2		
10 Ar + 5% N_2	26.2, 24.4, 25.3, 25.8, 26.2, 27.1, 24.4, 25.8	25.65		

ISSN No. 2454-6194 | DOI: 10.51584/IJRIAS |Volume XI Issue IX September 2026

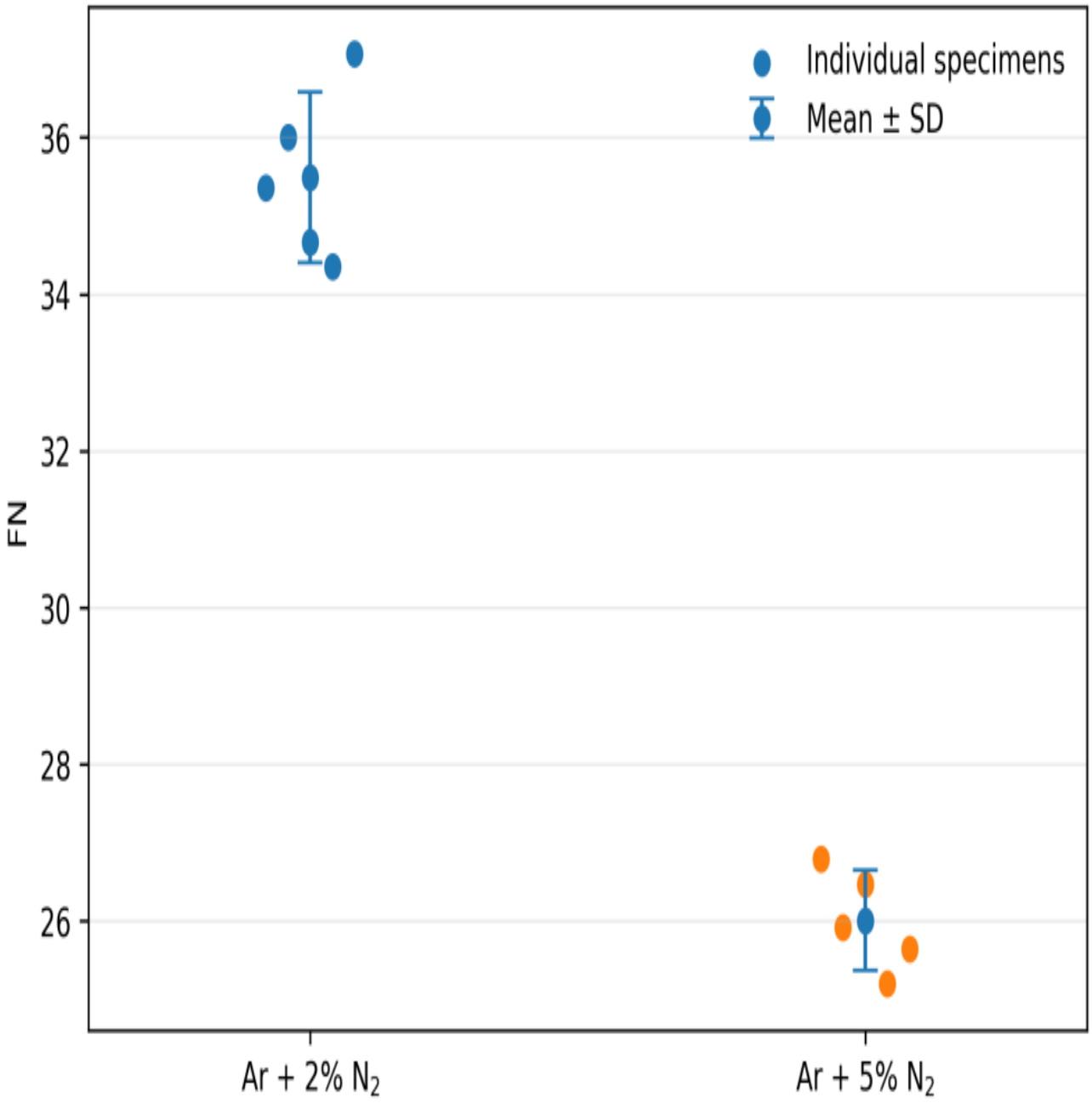

Fig. 10. Ferrite Number for the two processing groups. Points are coupon means from eight surface readings; markers with error bars show group mean ± sample SD.

Metallurgical interpretation of the optical microstructure

The optical micrographs at 200× and 500× show the characteristic heterogeneous duplex morphology of the deposited material, with elongated and plate-like constituents distributed within a continuous matrix. This appearance is consistent with the typical solidification behaviour of duplex stainless steel, where the weld metal solidifies mainly as ferrite and austenite forms during subsequent cooling and reheating. In multilayer CMT deposition, each new layer reheats the previously deposited material, which can further influence ferrite-to-austenite transformation and produce local variations in phase morphology. The elongated and lath-like features visible in several regions are consistent with austenite developing along ferrite boundaries and extending into the ferritic matrix. Since the present study is based on optical microscopy without quantitative image analysis, EBSD or phase-specific compositional mapping, the micrographs are used only for qualitative metallurgical interpretation, while the quantitative assessment of phase balance is based on the measured Ferrite Number.

ISSN No. 2454-6194 | DOI: 10.51584/IJRIAS |Volume XI Issue IX September 2026

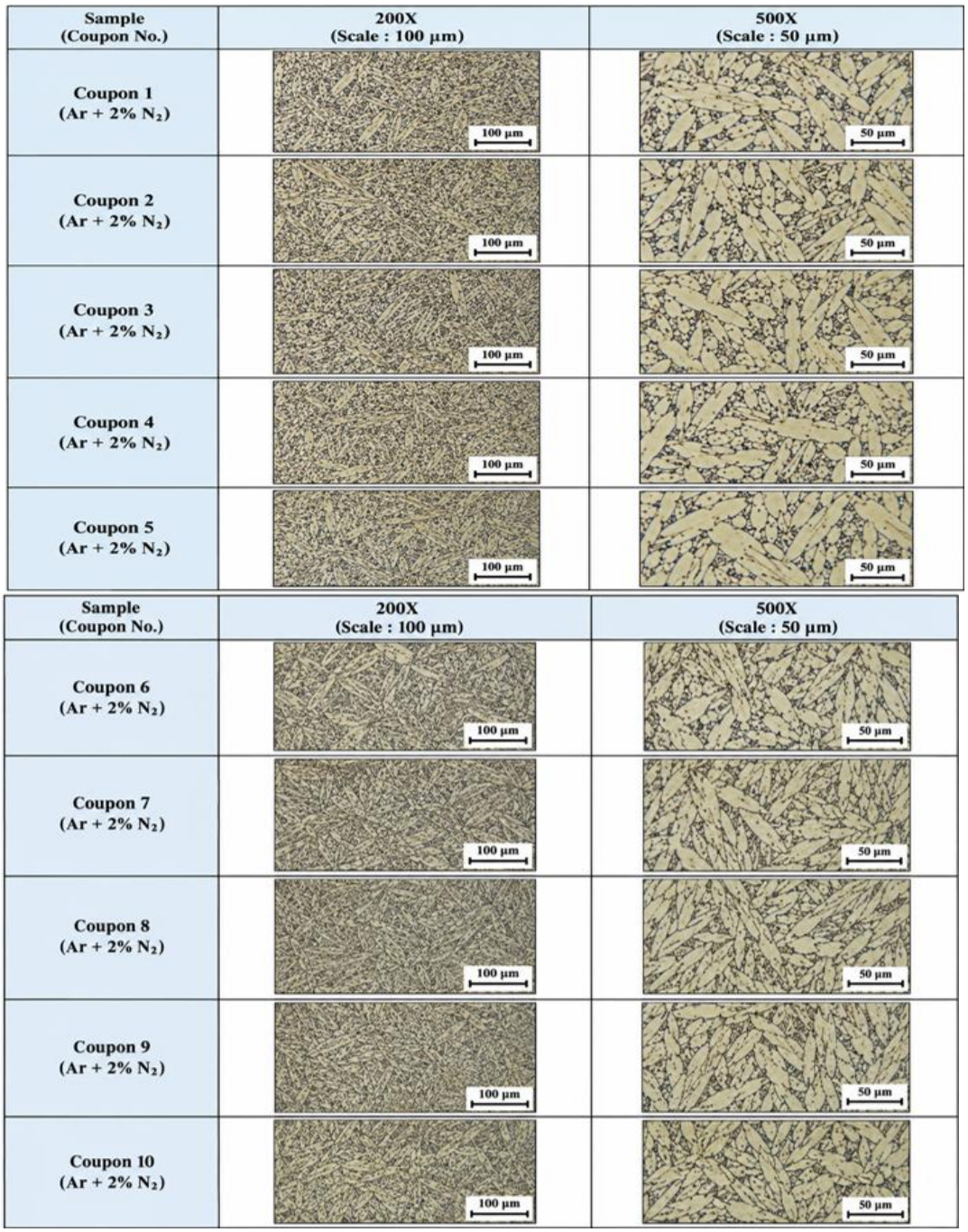

Fig.11. Optical microstructures of ER2209 multilayer CMT deposits recorded at 200× and 500× magnification, showing the characteristic duplex morphology. Scale bars: 100 µm at 200× and 50 µm at 500× for ten coupon.

Mechanical response

Vickers hardness

The coupon-average hardness values for the Ar + 2% N_2 processing group were 256.79, 255.38, 262.83, 271.50 and 271.92 HV10, giving a group mean of 263.68 ± 7.84 HV10. The corresponding values for the Ar + 5% N_2 group were 266.04, 266.63, 267.58, 256.08 and 254.75 HV10, resulting in a mean of 262.22 ± 6.25 HV10. The difference between the group means was only 1.46 HV10 (approximately 0.6%) and was not statistically significant (Welch's t-test, $p = 0.752$). Average hardness therefore remained essentially unchanged between the two processing groups, as shown in Fig. 12. This contrasts with the much larger and statistically significant separation observed in Ferrite Number, indicating that the phase-balance difference was not accompanied by a comparable change in the overall indentation-hardness response of the deposited material.

ISSN No. 2454-6194 | DOI: 10.51584/IJRIAS |Volume XI Issue IX September 2026

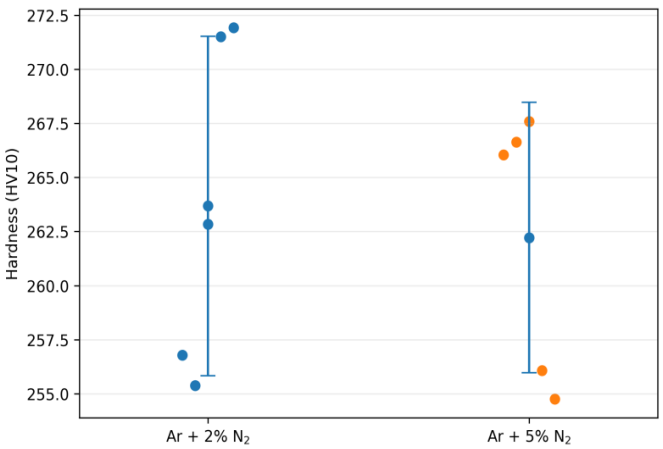

Fig. 12. Coupon-average Vickers hardness for the two processing groups (HV10). Error bars indicate group mean ± sample SD.

Impact energy

At 0 °C, the absorbed impact energies for the Ar + 2% N_2 processing group were 84, 90, 84, 68 and 62 J, yielding a mean of 77.6 ± 11.95 J. The corresponding values for the Ar + 5% N_2 group were 84, 82, 84, 98 and 96 J, with a mean of 88.8 ± 7.56 J. The latter group therefore showed a 14.4% higher mean absorbed energy. However, Welch's independent-samples t-test indicated that this difference was not statistically significant at $\alpha = 0.05$ ($p = 0.121$). The individual ranges (62–90 J and 82–98 J, respectively) also partially overlapped, as shown in Fig. 13. The higher mean impact energy is therefore interpreted as a trend within the present dataset rather than as a statistically established improvement. Its direction is consistent with the lower FN observed for the same processing group, although impact behaviour is also influenced by phase morphology, local heterogeneity, specimen orientation and thermal history.

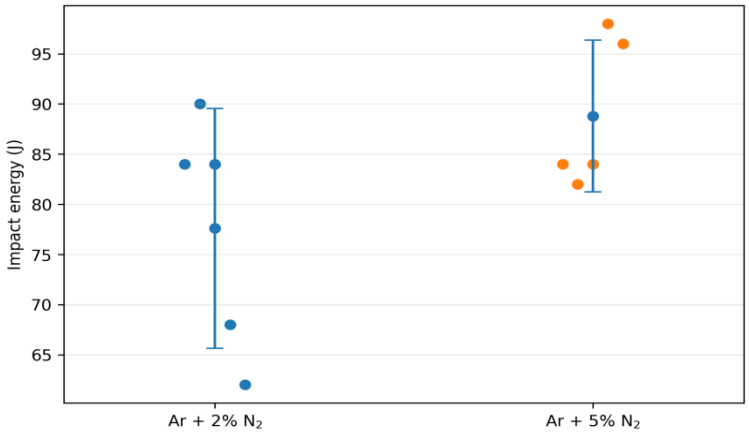

Fig. 13. Absorbed impact energy at 0 °C for the two processing groups. Points show individual specimens and error bars show group mean ± sample SD.

Tensile records and data-quality boundary

The Ar + 2% N_2 processing group exhibited UTS values of **812.96, 826.89, 788.40, 804.14 and 799.83 MPa**, corresponding to a mean of **806.44 MPa**. The associated elongation values gave a mean of **37.80%**. For the Ar + 5% N_2 group, three specimens exhibited UTS values of **842.24, 787.90 and 827.02 MPa**, whereas the remaining two tests produced substantially lower values of **113.59 and 588.64 MPa**. These lower strengths are consistent with the corresponding recorded peak loads and therefore cannot be attributed simply to a numerical unit conversion. Because no documented basis is presently available for classifying either test as invalid, the values are retained as recorded and a representative group-average UTS is not used for comparison between the two processing conditions.

The elongation values for the Ar + 5% N_2 specimens were **42.99, 44.82, 40.66, 43.96 and 42.01%**, giving a mean of **42.89%**. Although this mean is higher than that of the Ar + 2% N_2 group, the elongation trend is interpreted cautiously because two specimens in the same group exhibited anomalous tensile-load responses. Consequently, the tensile dataset is used primarily to document the measured range of behaviour rather than to support a quantitative claim of improved tensile strength under the Ar + 5% N_2 processing condition.

ASTM G48 mass-loss response

For the pitting-corrosion exposure, the Ar + 2% N_2 processing group produced mass-loss values of 0.443, 0.435, 0.590, 0.416 and 0.430 g/m², giving a mean of 0.4628 ± 0.0718 g/m². The corresponding values for the Ar + 5% N_2 group were 0.410, 0.364, 0.424, 0.526 and 0.498 g/m², with a mean of 0.4444 ± 0.0663 g/m². The mean value for the Ar + 5% N_2 group was only about 4.0% lower, the individual ranges overlapped substantially, and Welch's t-test showed no statistically significant difference ($p = 0.685$). In addition, no visible pits were reported during the post-test examination at approximately 20× magnification. The pitting test therefore indicates only a small difference in overall material loss between the two processing groups under the applied ASTM G48 exposure condition.

For the crevice-corrosion exposure, the Ar + 2% N_2 specimens exhibited mass-loss values of 0.712, 0.780, 0.540, 0.625 and 0.417 g/m², corresponding to a mean of 0.6148 ± 0.1428 g/m². The Ar + 5% N_2 group produced values of 0.391, 0.376, 0.278, 0.466 and 0.715 g/m², giving a mean of 0.4452 ± 0.1650 g/m² (Table 5). Thus, the mean mass loss of the Ar + 5% N_2 group was approximately 27.6% lower. Nevertheless, the difference did not reach statistical significance in Welch's t-test ($p = 0.121$). The lower mean is therefore treated as a trend requiring further replicated, matched-parameter validation rather than as a statistically established improvement due to shielding-gas nitrogen. No visible crevice attack was reported after exposure. Accordingly, the corrosion response is expressed as mass loss per unit area rather than as crevice depth, critical crevice temperature, or another localized-corrosion threshold.

Table 5. ASTM G48 mass loss per unit area (g/m²), mean ± sample SD.

Exposure	Ar + 2% N_2	Ar + 5% N_2	Difference in mean	Post-test observation
Pitting test	0.4628 ± 0.0718	0.4444 ± 0.0663	-4.0%	No visible pitting reported
Crevice test	0.6148 ± 0.1428	0.4452 ± 0.1650	-27.6%	No visible crevice attack reported

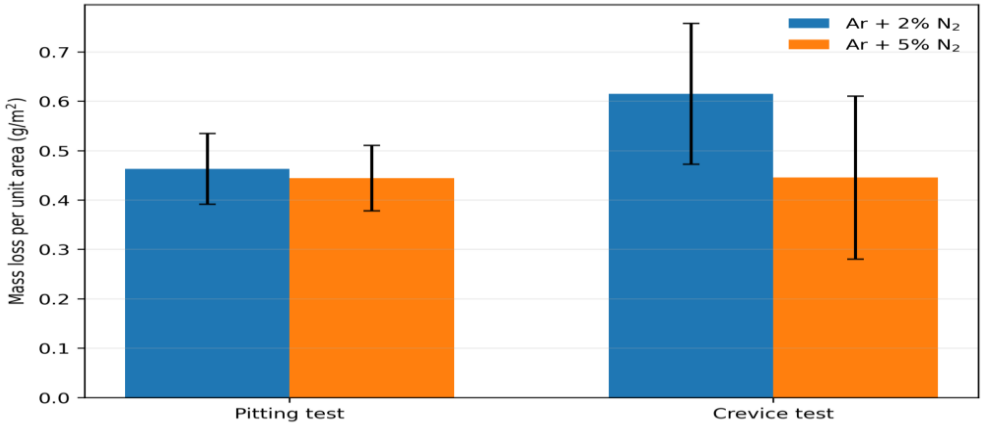

Fig. 14. ASTM G48 mass loss per unit area for the pitting and crevice tests. Bars show group mean and error bars show sample SD.

ISSN No. 2454-6194 | DOI: 10.51584/IJRIAS |Volume XI Issue IX September 2026

Statistical comparison of processing groups

Welch's independent-samples t-tests were performed using coupon-level values (n = 5 independent builds per processing group) as shown in table 6. Ferrite Number was the only principal response showing a statistically significant between-group difference at $\alpha = 0.05$. The remaining responses showed either negligible differences or numerical trends that did not reach statistical significance. These tests compare the complete processing groups; because shielding-gas composition was confounded with the deposition parameters and layer count, the p-values must not be interpreted as isolated nitrogen-concentration effects.

Table 6. Welch's t-test comparison of coupon-level responses between the two processing groups.

Response	Ar + 2% N_2 mean ± SD	Ar + 5% N_2 mean ± SD	Welch t	p-value	Interpretation
Ferrite Number (FN)	35.49 ± 1.09	26.01 ± 0.64	16.76	<0.001	Significant processing-group difference
Vickers hardness (HV10)	263.68 ± 7.84	262.22 ± 6.25	0.33	0.752	Not significant
Impact energy at 0 °C (J)	77.6 ± 11.95	88.8 ± 7.56	-1.77	0.121	Not significant; higher mean in Ar + 5% N_2 group
Pitting mass loss (g/m²)	0.4628 ± 0.0718	0.4444 ± 0.0663	0.42	0.685	Not significant
Crevice mass loss (g/m²)	0.6148 ± 0.1428	0.4452 ± 0.1650	1.74	0.121	Not significant; lower mean in Ar + 5% N_2 group

Note: Statistical significance indicates a difference between the two experimentally realized processing groups. It does not identify shielding-gas nitrogen concentration as an independent causal factor because the process variables and layer count were not matched.

Radiographic quality screening

Radiographic examination covered the full inspected length of the multilayer walls and was used as an internal-quality screening step before destructive characterization. The available radiographs did not show any extensive regions of gross volumetric porosity or other similarly large internal discontinuities. Some films contained locally marked indications; however, these cannot be classified without the original RT interpretation report and the applicable acceptance criteria. Radiography is therefore treated as a qualitative quality-control measure within the experimental workflow and is not used to rank the two shielding-gas processing groups or to establish code-based acceptance.

DISCUSSION

Phase balance under nitrogen-bearing shielding conditions

The Ferrite Number results provide the clearest metallurgical distinction between the two processing groups, and this was the only principal response that showed a statistically significant between-group difference in the present analysis ($p < 0.001$). Nitrogen is a strong austenite-stabilizing element in duplex stainless steel, and previous welding studies have shown that nitrogen-bearing shielding gases can promote austenite formation and modify phase-transformation behaviour [3][7]. Varbai and Májlinger demonstrated that the nitrogen content of duplex stainless-steel weld metal is influenced jointly by shielding-gas composition and heat input [6]. Similarly, Tóth et al. reported enhanced austenite formation during arc-based additive deposition with nitrogen-bearing

ISSN No. 2454-6194 | DOI: 10.51584/IJRIAS |Volume XI Issue IX September 2026

shielding gas, while also showing that arc power and travel speed remained important processing variables [10]. The substantially lower FN measured for the Ar + 5% N_2 processing group is therefore metallurgically consistent with the established role of nitrogen in promoting ferrite-to-austenite transformation, but statistical significance between the present processing groups should not be interpreted as proof that nitrogen concentration alone caused the observed magnitude of change.

The magnitude of this difference should nevertheless be interpreted in the context of the complete deposition history. The Ar + 5% N_2 walls contained **20 layers**, compared with **18 layers** for the Ar + 2% N_2 condition, and the two groups were produced using different combinations of current, voltage, travel speed and wire-feed speed. These differences influence melt-pool behaviour, cooling rate and cumulative reheating. In a multilayer deposit, repeated thermal cycling can modify the time available for austenite nucleation and growth from ferrite. Although the FN ranges for the two processing groups did not overlap and the mean FN was about 26.7% lower in the Ar + 5% N_2 group, this difference cannot be attributed only to the increase in nitrogen concentration in the shielding gas.

The OES results also call for a careful interpretation of the nitrogen data. Nitrogen measured in the deposited material ranged from 0.082 to 0.110 wt.%, which is lower than the 0.16 wt.% N reported for the ER2209 filler wire, and the values did not increase consistently with the nominal nitrogen content of the shielding gas. This may be related to dilution, nitrogen exchange in the molten pool, sampling position and differences in thermal history. Since nitrogen is not included among the principal analytes covered by ASTM E1086-22, these measurements are used only as supporting compositional data and not as definitive evidence of nitrogen uptake from the shielding gas. The change in phase balance is therefore considered to result from the combined influence of nitrogen availability, solidification behaviour, ferrite-to-austenite transformation kinetics and repeated thermal cycling, rather than from bulk nitrogen concentration alone.

Thermal history, heat input and layer count

The calculated heat input varied from 0.648 to 1.283 kJ/mm, which is almost a two-fold difference across the builds. Even so, heat input alone gives only a limited picture of the thermal history during multilayer deposition. Hosseini et al. reported that duplex stainless steel produced by WAAM can undergo different transformation histories under different interlayer conditions, with both the number and duration of reheating cycles influencing austenite formation and secondary-phase development [24]. In the present work, the 150 °C interpass limit helped to control heat accumulation, but using the same interpass threshold does not mean that all builds experienced the same thermal history. Peak temperature, cooling rate, dwell time, bead dimensions and the number of reheating cycles can still differ from one run to another. The importance of thermal exposure and cooling history in stainless-steel weldments has also been demonstrated by Gajjar et al., who reported that post-weld heat-treatment soaking time and cooling rate significantly affected sensitisation behaviour and chromium-depletion characteristics in Auto-TIG-welded austenitic stainless steel[25]. The coupling between heat input, microstructural evolution, hardness, mechanical behaviour and corrosion susceptibility has likewise been demonstrated in welded stainless-steel-containing joints, reinforcing the need to treat heat input as a metallurgically important process variable[26]. The sensitivity of stainless-steel weld microstructure and hardness to subsequent thermal exposure has also been reported during PWHT, where soaking time and cooling rate altered carbide precipitation and hardness evolution[27].

This becomes particularly important when the 18-layer and 20-layer walls are compared. The additional layers in the second group increase the deposition time and the number of reheating cycles, so differences in build height and phase balance cannot be considered separately from layer count. Similar observations have been reported in WAAM studies, where thermal path, build position and deposition strategy were linked with changes in microstructural uniformity[10], [11], [15], [18] To isolate the effect of shielding-gas composition more clearly in future work, the layer count and electrical and travel parameters should be kept constant, or a factorial experimental design should be used so that the effects of gas composition and thermal variables can be evaluated separately.

Mechanical response: toughness changes more than hardness

The mechanical results are easier to interpret when both effect size and statistical uncertainty are considered. Hardness showed almost no change between the two groups, with the mean values differing by less than 1%, and this difference was not statistically significant ($p = 0.752$). Impact energy was 14.4% higher on average in the Ar + 5% N_2 processing group, but the difference was also not statistically significant at $\alpha = 0.05$ ($p = 0.121$). A lower FN and a more austenite-favoured duplex balance can reasonably support strain accommodation and energy absorption, but impact behaviour is not controlled by phase balance alone. Notch orientation, inclusions, internal discontinuities, local microstructure and specimen extraction position can all influence the measured impact energy, especially in a directionally deposited wall. Similar concerns have been reported in recent CMT/WAAM studies. Bi et al. observed changes in microstructure and texture with build height in CMT-WAAM 2205 [6]. Tang et al. and Chen et al. reported marked mechanical anisotropy in CMT/WAAM duplex stainless steels, related to deposition direction, surface condition and microstructure [10], [11]. Bercelli et al. also showed that local deformation behaviour is strongly affected by the WAAM microstructure [12]. The present impact data therefore indicate a higher mean response in the second processing group under the specific test condition, but they do not establish a universal toughness improvement caused by 5% N_2 shielding gas.

The tensile results require separate consideration. An earlier summary indicated a modest increase in UTS, but two records from the second specimen set contain load values that do not reproduce that result. These records cannot be excluded without a documented technical reason. The elongation values are therefore retained and discussed descriptively, while no group-level UTS improvement is claimed. Verification of the original machine traces, fracture locations and specimen identities would be needed before the tensile-strength comparison could be reinstated in the final analysis.

Localized-corrosion response

Corrosion response in stainless-steel weldments is strongly dependent on thermal history and associated microstructural evolution; for example, PWHT studies on austenitic stainless steel have demonstrated changes in sensitisation/desensitisation through variations in soaking time and cooling rate[25].The corrosion results did not follow the Ferrite Number trend as clearly. In the pitting test, the difference between the two group means was only about 4% and was not statistically significant ($p = 0.685$), which is small compared with the variation within each group. This is reasonable because localized corrosion is controlled by the most vulnerable microstructural region rather than by the overall FN value alone. The distribution of Cr, Mo and N between ferrite and austenite, together with secondary austenite or nitride formation, oxide condition, inclusions and local surface preparation, can all influence where corrosion begins [3]–[5]. Since no visible pits were observed after testing, the small difference in total mass loss should not be overstated.

A more noticeable numerical difference was found in the crevice-corrosion test, where the mean mass loss for the Ar + 5% N_2 processing group was 27.6% lower. However, this difference was not statistically significant at $\alpha = 0.05$ ($p = 0.121$). ASTM G48 is used as a comparative chloride test for assessing pitting and crevice-corrosion resistance, so the observed difference remains relevant as a dataset-level trend under the applied test conditions[28]. Even so, it must be interpreted as a response associated with the overall processing group rather than with shielding-gas composition alone. The build parameters, layer count and phase balance all differed simultaneously, and the retained record does not provide the method letter, exposure temperature or duration needed for comparison with other laboratories. The present evidence therefore supports a lower average crevice-test mass loss in the second group, not a statistically established or universal corrosion improvement attributable solely to nitrogen concentration.

Relationship between chemistry, phase balance and properties

A useful feature of the dataset is that phase balance, hardness, impact energy and corrosion response were measured on material from the same overall campaign. Taken together, the measurements do not support a single-variable chain in which shielding-gas nitrogen determines bulk nitrogen, which determines FN, which

then determines every property. Instead, the strongest observation is the statistically significant processing-group separation in FN. Hardness did not differ significantly, while impact energy and crevice-test mass loss showed directionally favourable mean shifts that did not reach statistical significance, and pitting-test mass loss changed only slightly. Such a mixed response is consistent with a process-structure-property system in which different properties are sensitive to different microstructural length scales, local features and thermal histories.

This interpretation also fits published ER2209 and duplex-WAAM work. Karunanithi et al. linked WAAM microstructure to anisotropic mechanical and electrochemical performance [9], and Queguineur et al. demonstrated that filler chemistry and process variables jointly influence ferrite content and wall geometry[18]. Large-scale work by Mahey et al. reported broad uniformity in parts of a DSS 2209 WAAM build but also localized microstructural differences and tensile anisotropy [15]. The current study adds a shielding-gas comparison within a CMT multilayer window, but it should be viewed as complementary to—not a replacement for—matched-parameter experiments.

Limitations and inference boundary

Several limitations need to be acknowledged. The principal limitation is that shielding-gas composition changed together with current, voltage, travel speed, wire-feed speed and layer count, so the experiment compares two complete processing groups rather than a single isolated variable. In particular, the Ar + 2% N_2 walls contained 18 layers, whereas the Ar + 5% N_2 walls contained 20 layers, introducing a systematic difference in the number of reheating cycles. Consequently, even a statistically significant group difference cannot by itself establish shielding-gas nitrogen concentration as the causal factor. The substrate-grade certificate and the certificate for the Ar + 2% N_2 gas mixture were also not available in the present data records. In addition, some optical-microscopy preparation details and one micrograph-sheet heading still require traceability checks. Ferrite measurements were carried out using ASTM A800/A800M-20, which is intended for cast stainless steels; in this study, those values are used only for comparative magnetic assessment, while ISO 8249 is the weld-specific reference framework. The OES report also includes nitrogen values, although nitrogen is not listed within the scope of ASTM E1086-22. Two tensile-load records remain unresolved, and the available ASTM G48 documentation does not include the specific method letter or full exposure conditions.

Despite these limitations, several measured associations are internally consistent. The FN separation is large, reproducible at coupon level and statistically significant; hardness is statistically similar between the groups; impact energy is higher on average in the second group but does not reach statistical significance; pitting mass loss differs only slightly; and crevice mass loss is lower on average but likewise does not reach statistical significance. The manuscript therefore confines its conclusions to processing-group associations and avoids describing Ar + 5% N_2 as a universal optimum. A dedicated validation experiment should use identical current, voltage, travel speed, wire-feed speed, interpass-temperature criterion and layer count for both shielding-gas compositions, with independent replicate builds for each condition. Such a design would allow the specific contribution of shielding-gas nitrogen concentration to be separated from the accompanying thermal and deposition variables.

CONCLUSIONS

ER2209 multilayer CMT deposits produced under nominal Ar + 2% N_2 and Ar + 5% N_2 shielding conditions showed measurable differences in phase balance and selected performance characteristics. Since welding current, voltage, travel speed, wire-feed speed, heat input, and layer count were not fully matched between the two groups, the observations should be treated as processing-group differences rather than as the isolated effect of shielding-gas nitrogen concentration.

Ferrite Number showed the clearest separation between the two processing groups. The Ar + 2% N_2 group gave an average of 35.49 ± 1.09 FN, whereas the Ar + 5% N_2 group gave 26.01 ± 0.64 FN. This was the only measured response that showed a statistically significant difference between the groups. The lower FN observed for the Ar

+ 5% N_2 condition is consistent with the austenite-stabilizing role of nitrogen, although the contribution of the different thermal and deposition conditions cannot be separated in the present experimental design.

1. Average Vickers hardness remained nearly unchanged between the two groups, with values of 263.68 ± 7.84 and 262.22 ± 6.25 HV10. Mean impact energy at 0 °C increased from 77.6 ± 11.95 J for Ar + 2% N_2 to 88.8 ± 7.56 J for Ar + 5% N_2. However, the impact-energy difference was not statistically significant and is therefore regarded as a trend within the present dataset rather than a confirmed improvement.

2. The ASTM G48 pitting-test mass loss showed only a small difference, changing from 0.4628 ± 0.0718 to 0.4444 ± 0.0663 g/m². Crevice-test mass loss showed a larger reduction in the Ar + 5% N_2 processing group, from 0.6148 ± 0.1428 to 0.4452 ± 0.1650 g/m². Neither corrosion response showed a statistically significant difference between the groups, and no visible pitting or crevice attack was reported during the post-test examination.

3. OES results indicated comparatively stable Cr–Ni–Mo chemistry across the deposited material. The reported nitrogen content ranged from 0.082 to 0.110 wt.%, but these values are used only as supporting compositional information and not as direct evidence of nitrogen uptake from the shielding gas, because the analytical method and unmatched thermal conditions do not allow such a conclusion.

4. The tensile results were not used to establish a group-level strength difference because two specimens from the Ar + 5% N_2 set showed unusually low recorded tensile-load responses for which no documented basis for exclusion was available. The tensile data are therefore retained only as descriptive results.

5. Overall, the Ar + 5% N_2 processing group was associated with lower Ferrite Number, higher mean impact energy, and lower mean crevice-test mass loss. Of these responses, only Ferrite Number showed a statistically significant group difference. A follow-up study using the same current, voltage, travel speed, wire-feed speed, heat input, interpass-temperature criterion, and layer count for both shielding-gas conditions, together with independent replicate builds, would allow the specific contribution of nitrogen concentration to be evaluated more reliably.

Funding

This research was conducted without specific funding from any grant-awarding organization.

Disclosure statement

The author confirms the absence of any potential conflicts of interest.

Acknowledgement

The author acknowledges Tata IIS (welding), Anup Engineering Ahmedabad (testing) for their contributions, which included welding and testing.

REFERENCES

1. J. Verma and R. V. Taiwade, “Effect of welding processes and conditions on the microstructure, mechanical properties and corrosion resistance of duplex stainless steel weldments—A review,” *J. Manuf. Process.*, vol. 25, pp. 134–152, 2017, doi: https://doi.org/10.1016/j.jmapro.2016.11.003.
2. V. A. Hosseini, M. Högström, K. Hurtig, M. A. V. Bermejo, L.-E. Stridh, and L. Karlsson, “Wire-arc additive manufacturing of a duplex stainless steel: thermal cycle analysis and microstructure characterization,” *Weld. World*, vol. 63, no. 4, pp. 975–987, 2019, doi: 10.1007/s40194-019-00735-y.
3. P. K. Gajjar, B. C. Khatri, A. M. Siddhpura, and M. A. Siddhpura, “Sensitization and Desensitization (Healing) in Austenitic Stainless Steel: A Critical Review,” *Trans. Indian Inst. Met.*, vol. 75, no. 6, pp. 1411–1427, 2022, doi: 10.1007/s12666-021-02439-8.

4. Z. Zhang, H. Jing, L. Xu, Y. Han, L. Zhao, and C. Zhou, "Effects of nitrogen in shielding gas on microstructure evolution and localized corrosion behavior of duplex stainless steel welding joint," *Appl. Surf. Sci.*, vol. 404, pp. 110–128, 2017, doi: 10.1016/j.apsusc.2017.01.252.
5. A. Muñoz, J. Antón, J. Guiñón, and V. Pérez-Herranz, "Effect of Nitrogen in Argon as a Shielding Gas on Tungsten Inert Gas Welds of Duplex Stainless Steels," *Corrosion*, vol. 61, pp. 693–705, Jul. 2005, doi: 10.5006/1.3278204.
6. X. Y. Zhang, X. Q. Zha, L. Q. Gao, P. H. Hei, and Y. F. Ren, "Influence of shielding gas on microstructure and properties of gmaw dss2205 welded joints," *Materials (Basel).*, vol. 14, no. 10, pp. 1–15, 2021, doi: 10.3390/ma14102671.
7. N. M. Bhangale *et al.*, "Influence of shielding gas composition on nitrogen retention , phase balance , and corrosion performance of super-duplex stainless steel weld overlays produced by mechanised GMAW corrosion performance of super-duplex stainless steel weld overlays produced," *Can. Metall. Q.*, vol. 4433, pp. 1–17, 2026, doi: 10.1080/00084433.2026.2725450.
8. B. Varbai and K. Májlinger, "Physical and theoretical modeling of the nitrogen content of duplex stainless steel weld metal: Shielding gas composition and heat input effects," *Metals (Basel).*, vol. 9, no. 7, 2019, doi: 10.3390/met9070762.
9. Z. Zhang, Y. Han, X. Lu, T. Zhang, Y. Bai, and Q. Ma, "Effects of N2 content in shielding gas on microstructure and toughness of cold metal transfer and pulse hybrid welded joint for duplex stainless steel," *Mater. Sci. Eng. A*, vol. 872, no. January, p. 144936, 2023, doi: 10.1016/j.msea.2023.144936.
10. X. Bi, R. Li, Z. Hu, J. Gu, and C. Jiao, "Microstructure and Texture of 2205 Duplex Stainless Steel Additive Parts Fabricated by the Cold Metal Transfer (CMT) Wire and Arc Additive Manufacturing (WAAM)," *Metals (Basel).*, vol. 12, no. 10, 2022, doi: 10.3390/met12101655.
11. Y. Yuan, R. Li, X. Bi, J. Gu, and C. Jiao, "Experimental and Numerical Investigation of CMT Wire and Arc Additive Manufacturing of 2205 Duplex Stainless Steel," 2022.
12. B. Tang *et al.*, "Mechanical properties, microstructure, and theoretical modeling of CMT-WAAM 2209 duplex stainless steel," *J. Constr. Steel Res.*, vol. 235, p. 109892, 2025, doi: https://doi.org/10.1016/j.jcsr.2025.109892.
13. M.-T. Chen *et al.*, "Experimental investigation on the tensile behavior of wire arc additively manufactured duplex stainless steel plates," *Eng. Struct.*, vol. 321, p. 118764, 2024, doi: https://doi.org/10.1016/j.engstruct.2024.118764.
14. L. Bercelli, C. Caër, M. Dhondt, C. Doudard, J. Beaudet, and S. Calloch, "Full-field measurements of the microstructure's effect on the mechanical behaviour of a wire and arc additively manufactured duplex stainless steel," *Mater. Des.*, vol. 244, p. 113223, 2024, doi: https://doi.org/10.1016/j.matdes.2024.113223.
15. V. Mahey, G. A. Johnson, P. Burad, R. Chulist, P. C. Collins, and S. Roy, "Large-scale wire arc additive manufacturing of duplex stainless steel: Comprehensive insights into microstructure and mechanical behavior," *Mater. Sci. Eng. A*, vol. 963, p. 150232, 2026, doi: https://doi.org/10.1016/j.msea.2026.150232.
16. P. K. Gajjar, B. C. Khatri, Y. Das, and R. Moat, "Mechanical and intergranular corrosion properties of auto TIG welded TP347H-T91 dissimilar weldments," *Mater. Sci. Technol. (United Kingdom)*, vol. 40, no. 7, pp. 503–516, 2024, doi: 10.1177/02670836231212612.
17. S. P. Karunanithi, R. K. Arasappan, and S. S. Nallathambi, "Microstructural Evolution, Mechanical and Electrochemical Performance of Duplex Stainless Steel Fabricated by Wire Arc Additive Manufacturing with ER2209 Filler Wire," *steel Res. Int.*, vol. 95, no. 12, p. 2400425, 2024, doi: https://doi.org/10.1002/srin.202400425.
18. A. Queguineur *et al.*, "Wire arc additive manufacturing of thin and thick walls made of duplex stainless steel," *Int. J. Adv. Manuf. Technol.*, vol. 127, no. 1–2, pp. 381–400, 2023, doi: 10.1007/s00170-023-11560-5.
19. T. Tóth, E. M. Westin, M. Köhler, and K. Dilger, "Enhancing austenite formation in directed energy deposition-arc fabrication of duplex stainless steel using nitrogen-bearing shielding gas," *Weld. World*, vol. 69, no. 3, pp. 837–848, 2025, doi: 10.1007/s40194-024-01914-2.
20. B. Patel, D. K. Patel, V. Badheka, and P. Gajjar, "Role of stirring direction in the microstructural and tribological behaviour of graphene-reinforced Al 6061-T6 surface composite using FSP," *Weld. Int.*, vol.

0, no. 0, pp. 1–13, 2026, doi: 10.1080/09507116.2026.2662007.
21. V. K. Patel, H. Rana, D. K. Patel, V. Badheka, and P. Gajjar, "Impact of innovative reinforcement strategies on microstructure, mechanical, and wear properties of magnesium-based surface composites produced by friction stir processing," *J. Compos. Mater.*, vol. 0, no. 0, pp. 1–17, 2026, doi: 10.1177/00219983261465760.
22. R. Oza, A. B. Dhruv, V. Badheka, K. Mehta, and P. Gajjar, "Ultrasonic-Assisted Stir Casting of Sic-Reinforced AA2024 Composites: Microstructure and Mechanical Properties," *Int. J. Met.*, 2026, doi: 10.1007/s40962-026-02110-2.
23. "Standard Test Methods for Pitting and Crevice Corrosion Resistance of Stainless Steels and Related Alloys by Use of Ferric Chloride Solution 1", doi: 10.1520/G0048-11R15.
24. V. A Hosseini, M. Högström, K. Hurtig, M. A. Valiente Bermejo, L. E. Stridh, and L. Karlsson, "Wire-arc additive manufacturing of a duplex stainless steel: thermal cycle analysis and microstructure characterization," *Weld. World*, vol. 63, no. 4, pp. 975–987, 2019, doi: 10.1007/s40194-019-00735-y.
25. P. K. Gajjar, B. C. Khatri, J. Vora, R. Jha, H. R. Prajapati, and M. V. Mehta, "Experimental investigation on the effect of post-weld heat treatment on intergranular corrosion properties of auto TIG-welded SA213 TP304 grade austenitic stainless steel: Étude expérimentale de l'effet du traitement thermique après soudage sur les propri," *Can. Metall. Q.*, vol. 65, no. 1, pp. 586–603, 2026, doi: 10.1080/00084433.2025.2487724.
26. P. Gajjar *et al.*, "Heat input–microstructure–corrosion relationship in auto TIG–welded joints between low-alloy steels (T12, T22, and T91) and austenitic stainless steel (TP347H)," *Weld. World*, 2025, doi: 10.1007/s40194-025-02223-y.
27. P. K. Gajjar, B. C. Khatri, and R. Jha, "Investigation of effect of post weld heat treatment on microhardness and microstructure of auto TIG welded stabilized SA213 TP347H weldments," *Weld. Int.*, vol. 38, no. 5, pp. 366–382, 2024, doi: 10.1080/09507116.2024.2342340.
28. "Standard Test Methods for Pitting and Crevice Corrosion Resistance of Stainless Steels and Related Alloys by Use of Ferric Chloride Solution 1", doi: 10.1520/G0048-11R20E01.